Royal Netherlands
Meteorological Institute
Ministry of Infrastructure and the Environment

CLARIFI
CLouds and Aerosol Radiative Interaction and Forcing Investigation

M. de Graaf, L.G. Tilstra and P. Stammes

De Bilt, 2012 | Scientific report; WR 2012-01

CLARIFI
CLouds and Aerosol Radiative Interaction and Forcing Investigation

Version 1.0

Date March 2012
Status Final

CLARIFI
CLouds and Aerosol Radiative Interaction and Forcing Investigation

M. de Graaf, L. G. Tilstra and P. Stammes

Royal Netherlands Meteorological Institute (KNMI)
De Bilt, The Netherlands

March, 2012

Contents

Summary

The CLouds and Aerosol Radiative Interaction and Forcing Investigation (CLARIFI) project was carried out as part of ESA's Changing Earth Science Network Initiative. The goal of the project was to quantify the radiative effect of ultraviolet (UV)-absorbing aerosols above clouds, using a new method based on space-based spectral reflectance measurements and radiative transfer modelling.

Aerosols play an important role in the global energy balance, by absorbing and scattering solar radiation, and more importantly, by modifying cloud properties and atmospheric column stability. These important secondary effects in the global energy balance are currently far from understood and CLARIFI was designed to help unravel an important part of this problem using existing satellite measurements.

The unique broad spectral range of the space-borne spectrometer Scanning Imaging Absorption Spectrometer for Atmospheric Chartography (SCIAMACHY) was used to separate aerosol radiative effects in the UV, and cloud radiative effects in the shortwave infrared (SWIR). In the UV, aerosol absorption from smoke is strong, creating a strong signal in the measured reflectance. In the SWIR, absorbing and scattering effects from smoke are negligible, allowing the retrieval of cloud parameters from the measured spectrum using existing retrieval techniques. The spectral signature of the cloud can be modelled using a radiative transfer model (RTM) and the cloud parameters retrieved in the SWIR. In this way, the aerosol effects can be determined from the measured aerosol-polluted cloud shortwave spectrum and the modelled aerosol-unpolluted cloud shortwave spectrum. The difference between the spectra are directly linked to the aerosol direct radiative effect (DRE), which can be quantified for each SCIAMACHY cloud scene. The aerosol DRE retrieved using this approach is not dependent on retrieved or assumed aerosol properties, which means a huge reduction in the uncertainty of the derived aerosol DRE as compared to existing methods.

During project CLARIFI a large LookUp Table (LUT) of precomputed cloud reflectance spectra was created for the fast computation of the aerosol DRE for SCIAMACHY cloud scenes. This LUT contains the shortwave reflectance spectra for a range of aerosol-unpolluted water clouds which are likely to be present under smoke layers. It was shown that this LUT can be used to simulate the reflectance spectrum of a SCIAMACHY cloud scene or other space-borne spectro(radio)meters. Using SCIAMACHY data, the aerosol DRE was quantified for a region over the South-Atlantic Ocean in the boreal summer months of 2006–2009, when smoke from vegetation fires is present over a persistent marine stratiform cloud deck. The aerosol DRE averaged through August 2006 was found to be 23 ± 8 Wm^{-2} with a mean variation over the region in this month of 22 Wm^{-2}. The largest aerosol DRE over clouds found in that month was 132 ± 8 Wm^{-2}, which is a significant portion of the incoming solar radiation, heating the atmosphere locally.

The results were presented at several workshops and conferences, and a paper was published in the peer-reviewed literature, describing the method and these results for the first time.

1. Introduction

The radiative effects of atmospheric aerosols potentially compensate for the increases in the effects of greenhouse gases, but the magnitude and even sign of their net effect is uncertain, due to their influences on clouds [e.g. *Haywood and Boucher*, 2000; *Lohmann and Feichter*, 2005]. This makes the aerosol climate effects one of the least certain components of global climate models [*Yu et al.*, 2006; *Forster et al.*, 2007]. Even the aerosol direct radiative effect (DRE), the component of aerosol climate forcing that neglects all influences on clouds, is still poorly constrained, due to the heterogeneous distribution of aerosol sources and sinks and the influence of clouds on global observations of aerosols. In particular, the characterisation of aerosol properties in cloud scenes has been proved challenging. Locally, the aerosol DRE can be very large and dominate the climate forcing.

Recently, many studies have focused on the southern African region to study the aerosol DRE over clouds, where annually recurring biomass burning events in the local dry season (June - September) produce light-absorbing aerosols that are advected over marine stratiform clouds [e.g. *Swap et al.*, 1996; *Herman et al.*, 1997; *Torres et al.*, 2002; *de Graaf et al.*, 2007]. Modelling studies of aerosol DRE differ in magnitude and sign, but all studies show that the DRE strongly depends on the underlying surface. Over dark surfaces like the ocean, the scattering effects of the aerosols dominate, leading to a negative DRE, while over bright surfaces and clouds the scene albedo is decreased due to aerosol absorption, leading to a less negative or positive DRE [*Keil and Haywood*, 2003; *Abel et al.*, 2005; *Tummon et al.*, 2010]. These results depend on the diurnal cycle of clouds [e.g. *Myhre et al.*, 2003], while semi-direct effects change the results and can even dominate the DRE [*Sakaeda et al.*, 2011]. The semi-direct effect is strongest for absorbing aerosols inside the boundary layer, but still significant for aerosol layers that are located above the boundary layer [*Johnson et al.*, 2004].

Over China, annually recurring rice straw burning also causes light-absorbing aerosols which are advected over the ocean and over clouds. The total upwelling shortwave flux as measured by Clouds and the Earth's Radiant Energy System (CERES) was found to be reduced by more than $100\ \mathrm{Wm}^{-2}$ over cloud scenes with high values of Total Ozone Mapping Spectrometer (TOMS) Aerosol Index (AI), indicating absorbing aerosol layers over the clouds [*Hsu et al.*, 2003].

All studies show a very strong dependence on aerosol microphysical properties. During the SAFARI2000 field campaign, valuable information on scattering properties of biomass burning aerosols over clouds were obtained from air-borne measurements [*Haywood et al.*, 2003]. On a global basis the retrieval of aerosol properties in the presence of clouds is challenging. Most current satellite aerosol retrieval algorithms rely on cloud screening before retrieving aerosol information [e.g. *Tanré et al.*, 1996; *Torres et al.*, 1998; *Veefkind et al.*, 2000; *Diner et al.*, 2001; *King*, 2003; *Hauser et al.*, 2005]. Therefore, studies of the aerosol indirect effects from space–based instruments are necessarily often restricted to aerosols in the vicinity of clouds [e.g. *Redemann et al.*, 2009; *Costantino and Bréon*, 2010]. However, in some cases cloud and aerosol information can be separated in the radiation received at the top-of-atmosphere (TOA). Absorbing aerosols reduce the scene reflectance in the UV and visible spectral region, which may be used to retrieve the spectral optical aerosol properties in individual cases by fitting the reflectance spectrum to model results [*de Graaf et al.*, 2007]. However, the large number of aerosol properties determining the reflectance spectrum will result often in multiple solutions. Aerosols also significantly affect the polarised light reflected by clouds under certain scattering geometries, which can be used to derive aerosol optical properties in cloudy scenes [*Waquet et al.*, 2009; *Knobelspiesse et al.*, 2011]. This can be used to derive aerosol DRE over clouds using space-borne polarimeter measurements. In the case of active remote sensing, like lidar, the atmospheric scattering properties are vertically resolved, allowing for separation of aerosol and cloud properties and the computation of aerosol DRE over clouds in a small but global track [*Chand et al.*, 2008; *Wilcox*, 2010]. Using space-borne lidar measurements, the aerosol DRE over marine clouds was found to change sign from negative to positive at a cloud fraction of 0.4, which can be used to constrain modelling results [*Chand et al.*, 2009]. Heating rates can be computed when aerosol vertical profiles are available. Using satellite cloud products and Ozone Monitoring Instrument (OMI) Aerosol Index (AI) [*Torres et al.*, 2007] as a proxy for aerosol presence, the liquid water path and thicknesses of clouds was found to increase from the presence of aerosols above the clouds and the subsequent heating of the atmosphere [*Wilcox*, 2011]. This implies a negative semi-direct radiative effect of the aerosols. In another more statistical study the OMI AI was found to decrease the local planetary albedo through the direct and first indirect effect, which allowed for the retrieval of the aerosol DRE in cloudy scenes in the tropical and sub–tropical oceans [*Peters et al.*, 2011]. The accuracy of these results are strongly influenced by the accuracy of the aerosol optical

and microphysical parameters that are used to represent the actual ambient aerosols.

During project CLARIFI the aerosol DRE over clouds was quantified over the South-Atlantic Ocean. A methodology was designed to quantify the aerosol DRE from the reflectance difference of measured aerosol-polluted cloud spectra from SCIAMACHY and modelled aerosol-unpolluted cloud spectra. This will be formally derived in section 2. The algorithm is illustrated in section 3, using SCIAMACHY measurements. The modelled cloud spectra were stored in LookUp Tables (LUTs), which are described in section 4.

2. Aerosol direct radiative effect over clouds

A radiative forcing or radiative effect of an atmospheric constituent x can be defined as the difference in the net irradiance ΔE at a certain level with and without the forcing constituent [e.g. *Forster et al.*, 2007; *Liou*, 2002]:

$$\Delta E_x = E^{\text{net}}_{\text{with } x} - E^{\text{net}}_{\text{without } x}, \tag{1}$$

where the net irradiance is defined as the difference between the downwelling and upwelling irradiances,

$$E^{\text{net}} = E^{\downarrow} - E^{\uparrow}. \tag{2}$$

Therefore, at the TOA, where the downwelling irradiance is the incoming solar irradiance E_0 for all scenes, the radiative effect of aerosols overlying a cloud is given by

$$\Delta E^{\text{TOA}}_{\text{aer}} = E^{\uparrow\ \text{TOA}}_{\text{cld}} - E^{\uparrow\ \text{TOA}}_{\text{cld + aer}}, \tag{3}$$

where $E^{\uparrow\ \text{TOA}}_{\text{cld}}$ is the upwelling irradiance at the TOA for an aerosol-free cloud scene and $E^{\uparrow\ \text{TOA}}_{\text{cld + aer}}$ is the upwelling irradiance for an aerosol-polluted cloud scene. By equation (3), if energy is absorbed in the atmosphere by the aerosols, the radiative forcing is positive.

The monochromatic irradiance $E(\lambda)$ can be found by integrating the monochromatic radiance $I(\lambda)$ over an entire hemisphere solid angle

$$E(\lambda) = \int_{\Omega} I(\lambda) \cos\Theta d\Omega, \tag{4}$$

which can be written in polar coordinates as

$$E(\lambda) = \frac{\mu_0 E_0(\lambda)}{\pi} \int_0^{2\pi} \int_0^1 R(\lambda, \mu, \phi; \mu_0, \phi_0) \mu d\mu d\phi, \tag{5}$$

where μ_0 is the cosine of the solar zenith angle, μ the cosine of the viewing zenith angle, and ϕ_0 and ϕ the azimuth angle of the incoming and outgoing beam relative to the scattering plane, respectively. $\mu_0 E_0$ is the TOA solar irradiance incident on a horizontal surface unit and R is the reflectance, defined as

$$R(\lambda) = \frac{\pi I(\lambda)}{\mu_0 E_0(\lambda)}. \tag{6}$$

The Earth's reflectance R at the TOA is the quantity measured by SCIAMACHY (first order product) and computed by a Radiative Transfer Model (RTM) for all levels. Below, R and all other quantities refer to quantities at the TOA.

The (local) plane albedo A for a scene is defined as the integral of R over all angles

$$A(\lambda, \mu_0) = \frac{1}{\pi} \int_0^{2\pi} \int_0^1 R(\lambda, \mu, \phi; \mu_0, \phi_0) \mu d\mu d\phi. \tag{7}$$

By substituting equation (7) in (5) and integrating over wavelength, the aerosol effect at the TOA (equation (3)) becomes

$$\Delta E_{\rm aer} = \int_0^\infty \mu_0 E_0 \left(A_{\rm cld} - A_{\rm cld\,+\,aer}\right) d\lambda. \tag{8}$$

For the simulated case the plane albedo can be obtained from the model results, by integrating the reflectances in all directions. However, for the measured case with clouds and aerosols, only the reflectance in the measured direction is known. Therefore, the plane albedo for this scene must be estimated.

A measure for the angular distribution of the scattering energy as a function of the scattering angle for a scene is the anisotropy factor B,

$$B = R/A. \tag{9}$$

Assuming that the anisotropy factors are the same for the clean and polluted cloud scenes, $B_{\rm cld} = B_{\rm cld\,+\,aer}$, equation (8) can be written as

$$\Delta E_{\rm aer} \simeq \Delta E_{\rm aer}^{\rm est} = \int_0^\infty \frac{\mu_0 E_0 \left(R_{\rm cld} - R_{\rm cld\,+\,aer}\right)}{B_{\rm cld}} d\lambda. \tag{10}$$

Equation (10) is used to derive the aerosol DRE over clouds from SCIAMACHY measurements of $R_{\rm cld+aer}$ and model results of $R_{\rm cld}$ and $B_{\rm cld}$.

3. Application to SCIAMACHY

The algorithm is illustrated in Figure 1. The SCIAMACHY reflectance spectrum observed on 13 August 2006, 09:19:43 UTC is shown in red. This is a typical measurement of a scene with smoke from the African continent that was advected over a marine low level cloud layer. The geometry for this scene was $[\theta, \theta_0, \phi - \phi_0] = [18.5°, 43.2°, 131.0°]$. The TOSOMI total ozone column Ω was 248 DU. The FRESCO cloud pressure and cloud fraction were 902 hPa and 0.6, respectively. The cloud droplet effective radius and cloud optical thickness, retrieved from the SWIR, were 11.2 μm and 14.4, respectively. With these parameters an aerosol-unpolluted cloud reflectance spectrum was

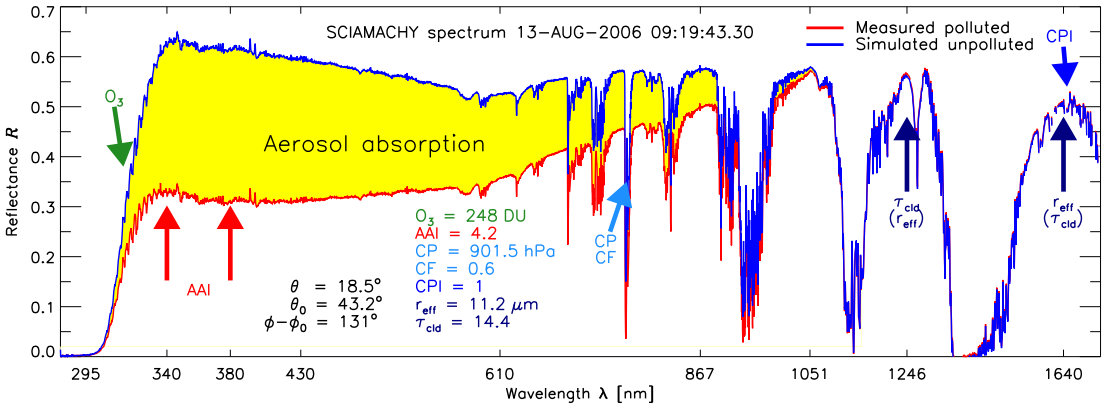

Figure 1: SCIAMACHY measured reflectance spectrum (red) on 13 August 2006, 09:19:43 UTC of the scene indicated by the arrow in Figure 4b; and the modelled equivalent unpolluted cloud reflectance spectrum (blue) for this scene. The difference between these two spectra (yellow, labelled 'Aerosol absorption') indicates the irradiance absorbed by the aerosols (see Figure 2). The parameters to model the cloud scene were retrieved at various parts of the spectrum (ozone (O3) between 325–335 nm, cloud fraction (CF) and cloud pressure (CP) at 760 nm, cloud phase index (CPI) around 1700 nm, cloud optical thickness ($\tau_{\rm cld}$) and effective radius ($r_{\rm eff}$) at 1246 and 1640 nm). The AAI is retrieved from the reflectances at 340 and 380 nm [*Tilstra et al.*, 2011].

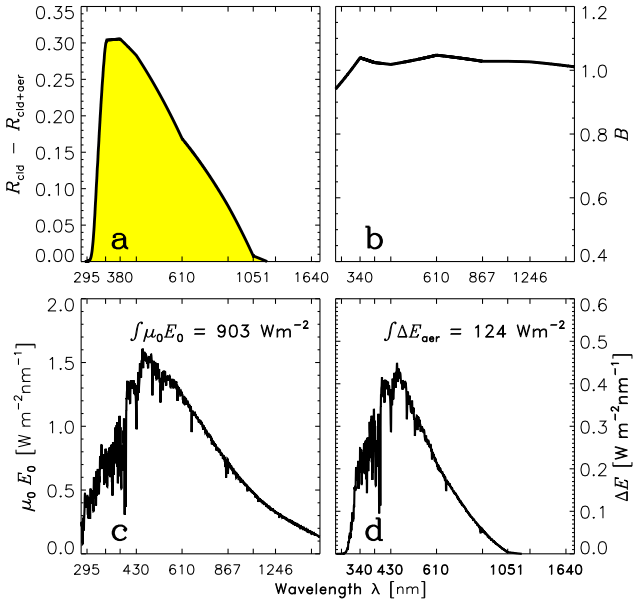

Figure 2: Various terms of equation (10) for the selected scene in Figure 4b. a) Reflectance difference between the blue and red curve in Figure 1. b) Anisotropy factor. c) Incoming solar irradiance for this scene. d) Irradiance absorbed by the aerosols above the clouds.

modelled, which is indicated by the blue curve. The measured and modelled spectra are close for wavelengths longer than 1246 nm, due to the assumption that the aerosol absorption optical thickness is negligible at these wavelengths. At wavelengths shorter than about 1100 nm, the reflectance spectra start to deviate, which is indicated by the yellow area. The difference increases with decreasing wavelength. This is caused by the aerosol absorption optical thickness, which increases with decreasing wavelength. At wavelengths below about 300 nm the differences disappear, because at these wavelengths the strong ozone absorption reduces the reflectance to zero. The aerosol absorption in the scene is confirmed by the high value of the AAI of 4.2.

The aerosol DRE over clouds for this scene was evaluated using equation (10). The various terms of this equation for the scene shown in Figure 1 are given in Figure 2 as a function of wavelength in the SCIAMACHY spectral range. The reflectance difference $(R_{\rm cld} - R_{\rm cld+aer})$ is given in Figure 2a, which is the same as the yellow area in Figure 1. It decreases with wavelength, except at those UV wavelengths where ozone absorption is so dominant that all radiation is absorbed. This term contains all the absorption effects in the scene which are not incorporated in the modelled cloud scene, and which are attributed to aerosol absorption. The anisotropy factor for the modelled cloud scene $B_{\rm cld}$ is plotted in Figure 2b; it is typically 0.8 - 1.0. The anisotropy factor for the aerosol-polluted cloud scene is not known, but a modelling study showed a change of less than 1% in aerosol DRE due to anisotropy changes from aerosol effects for scattering angles less than 60° (see section 5). The solar irradiance at TOA $\mu_0 E_0$ is given in Figure 2c. The total incident solar irradiance from 240 – 1750 nm can be obtained by integrating the given irradiance spectrum and was 903 Wm^{-2}. The spectral irradiance change due to aerosol absorption $(E_{\rm cld} - E_{\rm cld+aer})$ can be obtained by combining these three terms according to equation (10), and is plotted in Figure 2d. By integrating over wavelength the total aerosol DRE over clouds $\Delta E_{\rm aer}$ was found to be 124 Wm^{-2} for this scene. Note that the spectral range of SCIAMACHY covers 92% of the solar energy spectrum, which is sufficient to capture the entire spectral aerosol DRE over clouds. The aerosol DRE becomes zero due to ozone absorption of the radiation below 300 nm and it also becomes zero for wavelengths longer than 1246 nm, assuming that the aerosol absorption has become negligible around that wavelength. The integration over SCIAMACHY's spectral range does not introduce an additional error as long as the aerosol absorption has become negligible around 1750 nm.

3.1. Horizontal and vertical distribution of aerosols and clouds

The algorithm can be applied to any ocean scene that contains water clouds. This is illustrated in Figure 4. In August 2006 a two-week period of high AAI over clouds was observed over the South-Atlantic Ocean off the west coast of Namibia. These events can often be observed in this area from June to September, which is the local dry season. The high AAI values are caused by smoke from vegetation fires on the African mainland, which are advected over the Atlantic at altitudes of typically 1 - 5 km [e.g. *Herman et al.*, 1997; *Torres et al.*, 2002; *de Graaf et al.*, 2007].

A typical horizontal distribution of the cloud and aerosol fields off the west coast of Namibia is shown in Figure 4a and b, where SCIAMACHY CF and AAI measurements are overlaid on a MERIS RGB image. Clearly, the horizontal distributions of aerosols and clouds are very variable. Furthermore, they change rapidly from day to day.

The corresponding aerosol DRE field over marine clouds is shown in Figure 4c, for all scenes over the ocean, containing water clouds (CPI < 5) with effective cloud fractions greater than 0.3. It shows the unprecedented details of measured absorbed energy by aerosols over clouds. Clearly, the aerosol DRE is highly variable with location, dropping off to zero at the edges of the smoke field, corresponding with the AAI gradient. The maximum aerosol DRE over clouds measured by SCIAMACHY on this day is $124\ \mathrm{Wm}^{-2}$, indicated by the arrow. The measured reflectance spectrum for this scene was given in Figure 1. The minimum DRE was less than 0, which is not an indication of a negative aerosol DRE, but caused by the uncertainty of the measurements. The scale is cut at $-1\ \mathrm{Wm}^{-2}$, indicating that the aerosol DRE has vanished and aerosol-unpolluted clouds remain.

The vertical configuration for the event in Figure 4 is shown using a spatially closely collocated CALIPSO overpass. The CALIOP 532 nm and 1064 nm backscatter signals shown in Figure 3 were acquired during the night eight hours before the Envisat overpass. They show the strongly reflecting cloud layer at around 1 km altitude and the vertically extensive smoke layer between about 1 and 5 km altitude. The red arrows indicate the location of the white dot in Figure 4, where the AAI reaches the high value of 4.2. Clearly, clouds are overlain by absorbing aerosols, causing the high AAI value and the strong aerosol DRE at this point.

3.2. Regional monthly averaged aerosol DRE over clouds

The regionally averaged aerosol DRE over marine clouds was determined over the South-Atlantic Ocean between 20°S – 10°N and 10°W – 20°E in August 2006, see Figure 5. In this month a period of strong biomass burning was observed from about 10 – 21 August. Only water cloud scenes were averaged. Clear-sky scenes and scenes with ice clouds were discarded, by allowing only scenes with cloud fraction higher than 0.3, cloud pressures higher than 700 hPa and cloud phase index

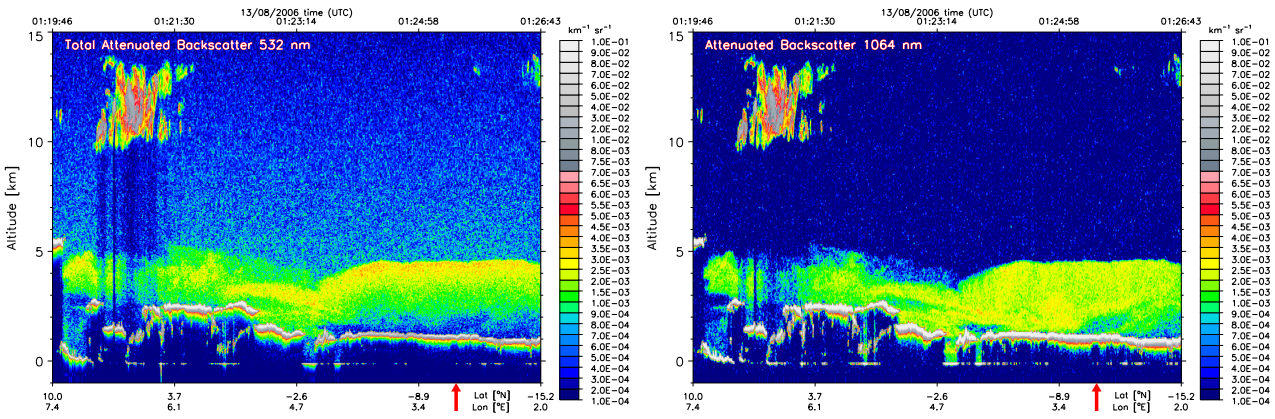

Figure 3: CALIOP 532 nm backscatter signal, on 13 August 2006, from 01:19:46 – 01:26:43 UTC, showing the vertical distribution of aerosols between 1–5 km (yellow/green) above the clouds at around 1 km (gray), along the CALIPSO track marked in white in Figure 4b. The red arrow corresponds to the white dot in the track in Figure 4b.

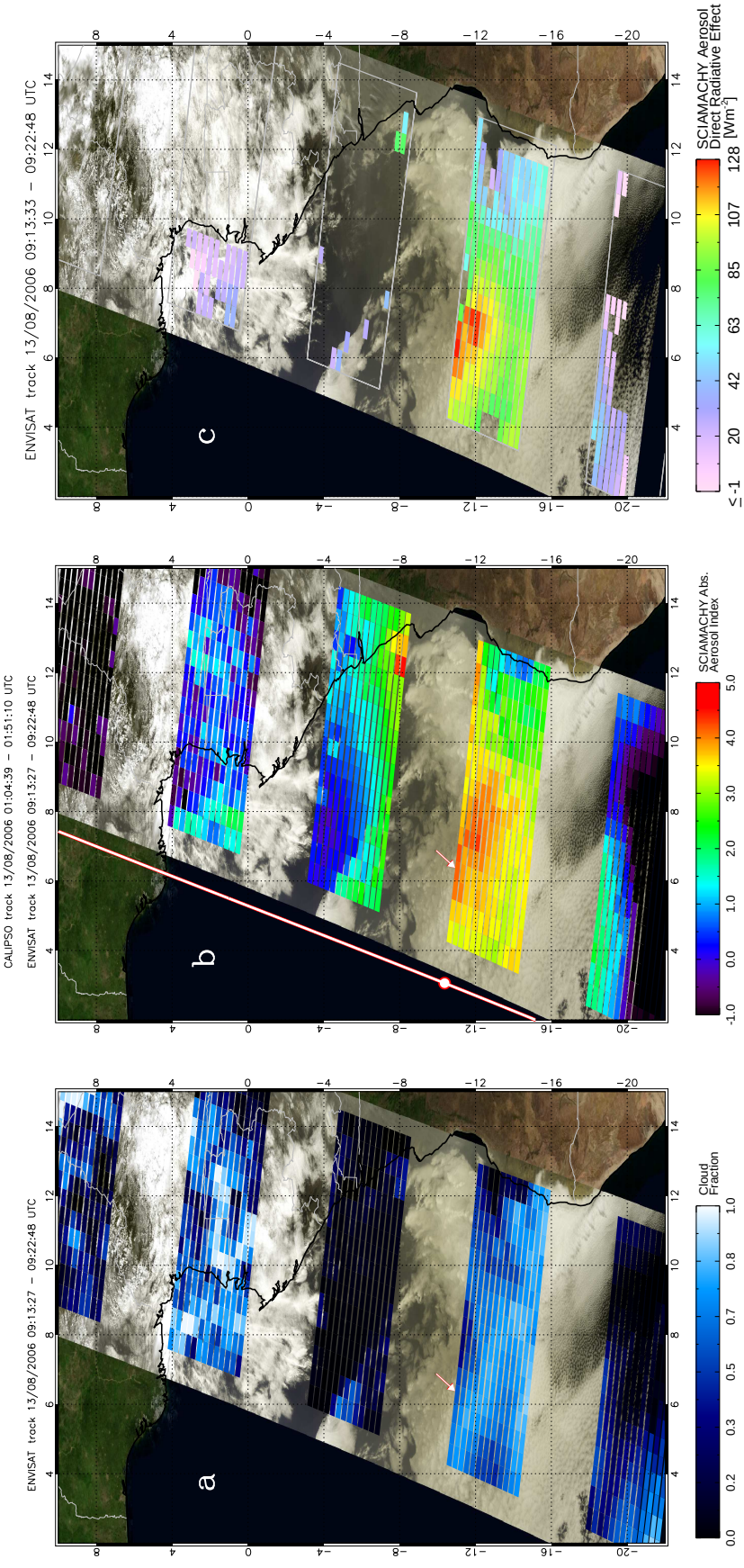

Figure 4: MERIS RGB composite showing the horizontal cloud distribution over the west coast of Africa on 13 August 2006, from 09:13:27 – 09:22:48 UTC, overlaid with a) SCIAMACHY/FRESCO effective cloud fraction; b) SCIAMACHY Absorbing Aerosol Index; c) SCIAMACHY Aerosol Direct Radiative Effect [Wm^{-2}], retrieved over marine clouds only. This shows the horizontal distribution of smoke over clouds over the Atlantic and the subsequent positive DRE due to the absorption of radiation by the aerosols over the clouds. The vertical distribution of clouds and aerosols along the white CALIPSO track in Figure 4b is shown in Figure 3. The distance between the CALIPSO track and the selected pixel (shown by the arrow) is 300 km. The aerosol absorption in the selected pixel is analysed in Figures 1 and 2.

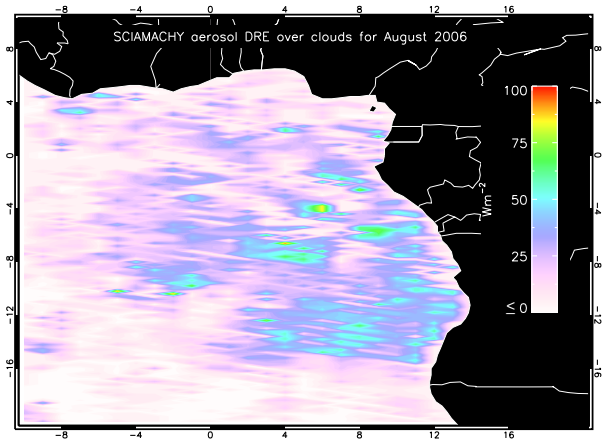

Figure 5: Monthly averaged aerosol DRE over marine clouds (CF > 0.3, CP > 700 hPa, CPI < 5) measured by SCIAMACHY in August 2006 over the South-Atlantic Ocean between 20°S and 10°N and 10°W and 20°E. Note that complete spatial coverage of SCIAMACHY nadir measurements is only once per six days. Therefore, gridbox values are averages of about 4 – 5 SCIAMACHY measurements.

below 5. No selection on aerosol amount was made. Figure 5 shows variations in the aerosol DRE over clouds, which has never been shown before using actual measurements. Some of the structures are caused by the low sampling of SCIAMACHY, but most is due to the variable cloud and aerosol fields, which change rapidly in days and even within one day.

The maximum DRE over clouds in a SCIAMACHY pixel in August 2006 was 132 ± 8 Wm^{-2}, and the regionally and monthly average of the aerosol DRE over clouds in August was 23 ± 8 Wm^{-2} with a standard deviation during this month of 22 Wm^{-2}.

The aerosol DRE was determined over the South-Atlantic Ocean during 2006–2009. Histograms of the data are shown in Figure 6, for July 2006 and July 2007. Although the average aerosol forcing over clouds is rather similar for these months, there are clear differences evident from the histograms. In 2006 more extreme events are visible, with cloud scenes having more than 100 Wm^{-2} of solar radiation absorption by aerosols. This kind of detail is only reached based on measurements. These events can be important in future studies of aerosol semi-direct effects on clouds, which can now be easily selected from the data.

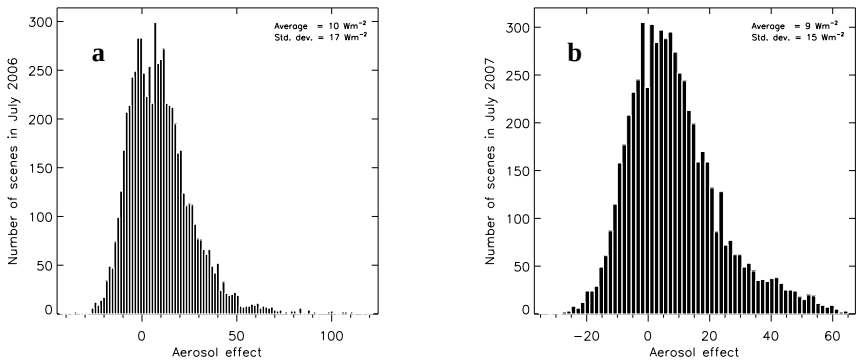

Figure 6: Histograms of aerosol DRE over clouds in the South-Atlantic region for a) July 2006 and b) July 2007.

Table 1: Spectral cloud reflectance LookUp Table nodes

Parameter	Nodes									
wavelength λ [nm]	295	310	340	380	430	610	867	1051	1246	1640
cloud optical thickness $\tau_{\rm cld}$	2	4	8	12	16	20	24	32	48	
droplet size $r_{\rm eff}$ [μm]	3	4	6	8	12	16	20	24		
cloud base height $z_{\rm cld}$ [km]	0	1	4	8	12					
total O_3 column Ω [DU]	267	334	401							
surface albedo $A_{\rm s}$	0	0.5	1							
droplet size eff. variance $\nu_{\rm eff}$	0.15									
number of θ_0, θ, $\phi - \phi_0$	36	36	19							

4. Modelled Cloud Shortwave Reflectance Spectra

In order to simulate aerosol–free cloud reflectance spectra, LUTs of TOA reflectances have been generated. With these LUTS aerosol DRE over clouds can be derived for SCIAMACHY pixels directly. The Doubling-Adding KNMI (DAK) RTM [*Stammes*, 2001] was used for the simulations of the reflectances. DAK computes the vectorised monochromatic reflectance and transmittance of a pseudo-spherical atmosphere, using the polarised doubling-adding method [*De Haan et al.*, 1987]. The internal radiation field of the atmosphere is determined in a finite number of layers, each of which can have Rayleigh scattering, gas absorption, and aerosol and cloud particle scattering and absorption. The atmosphere was divided in 32 layers, simulating a standard mid-latitude atmosphere gas and temperature profile [*Anderson et al.*, 1986]. The standard ground pressure was 1013 hPa. Water clouds were simulated in a 1 km thick layer using a gamma-distribution with effective radii varying between 4 and 16 microns and an effective variance of 1.5. This value is between typical values for stratus and stratocumulus [*Hansen*, 1971]. Cloud optical thickness $\tau_{\rm cld}$ ranged from 2 to 48. Only water clouds were modelled, which are the most likely ones encountered when aerosols overlie the cloud. However, the height of the clouds was not restricted to lower levels alone; the height of the cloud bottom ranged from 0 to 12 km. The TOA reflectance was computed at between $60^2 \times 19$ to $150^2 \times 19$ different geometries, depending on the required resolution in the RTM. This was scaled down to 36^2 solar and viewing angles and 19 azimuth angles for all model scenes. The surface albedo is accounted for analytically, by assuming it Lambertian and separating the contribution to the TOA reflectance from the surface and the atmosphere [cf. *Chandrasekhar*, 1960; *de Graaf et al.*, 2005]. In that case three surface albedo nodes suffice in the LUT. Table 1 lists all the 3.2×10^4 nodes of the LUT, each simulating cloud scene reflectances at 2.5×10^4 geometries.

An example of the modelled cloud scene TOA reflectances is shown in Figure 7. It shows the main dependencies of cloud reflectance spectra, which are $\tau_{\rm cld}$ (see the different curves in the plots) and surface albedo (compare top and bottom panels). At SWIR wavelengths the cloud droplet size starts playing a role due to absorption by fluid water. This increases with increasing $\tau_{\rm cld}$ and increasing cloud droplet size (compare left plots ($r_{\rm eff} = 4\mu$m) and right plots ($r_{\rm eff} = 16\mu$m)). The TOA reflectance of a cloud scene is almost independent on the height of the cloud base (not shown). At visible and UV wavelengths the effect of a changing ozone column density can be observed in green.

The LUT was generated for 10 wavelengths in the shortwave domain, and used to derive aerosol DRE from SCIAMACHY. However, the algorithm is not restricted to one instruments. It can be used to simulate the shortwave reflectance spectrum of water clouds, which may be compared to measurements from spectro(radio)meters or a combination of instruments sampling the shortwave spectrum. Examples include OMI+MODIS on the Aura and Aqua platforms, flying synchronous in the A-train, and the future missions of TROPOMI and VIIRS (on ESA satellite and NOAA NPP) and a combination of OMI and the future UV-NS on Metop-SG.

5. Accuracy

5.1. Unpolluted cloud spectra accuracy assessment

The LUTs described in the previous section also provide an independent calibration tool for satellite measurements of unpolluted (aerosol-free) cloud reflectance spectra. One example of a modelled and a measured unpolluted cloud reflectance spectrum is shown in Figure 8. The measured cloud reflectance spectrum on 14 August 2006 at 10:30:04 UTC over the South-Atlantic Ocean is shown in various colours, according to different integration times (IT) of SCIAMACHY. Parts of the spectrum

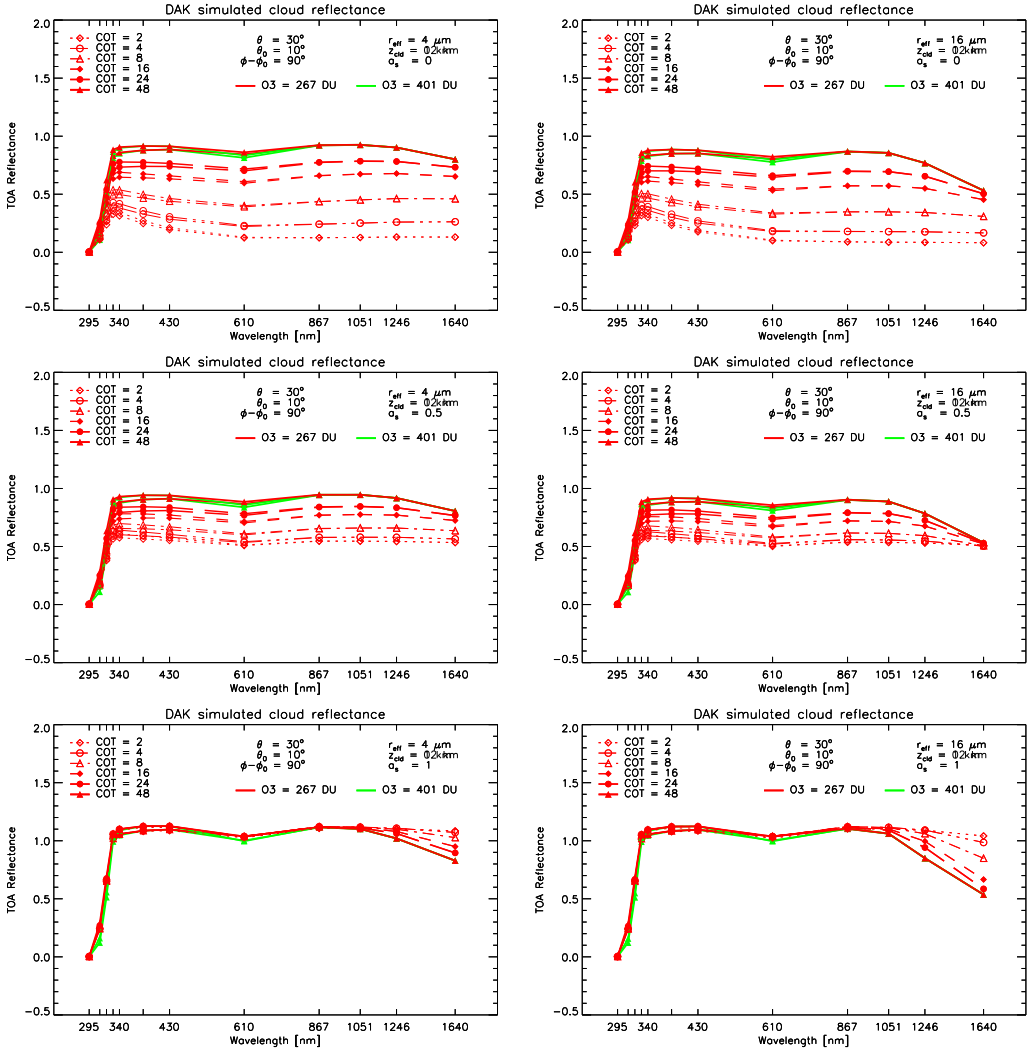

Figure 7: Subset of the LUT showing water cloud scene reflectance spectra for one geometry, a cloud base height of 0 km, a total ozone column of 267 DU and varying τ_{cld} , cloud droplet size and surface albedo (red). The green curve shows the water cloud scene reflectance spectra for a τ_{cld} of 48, but with the total ozone column changed to 401 DU.

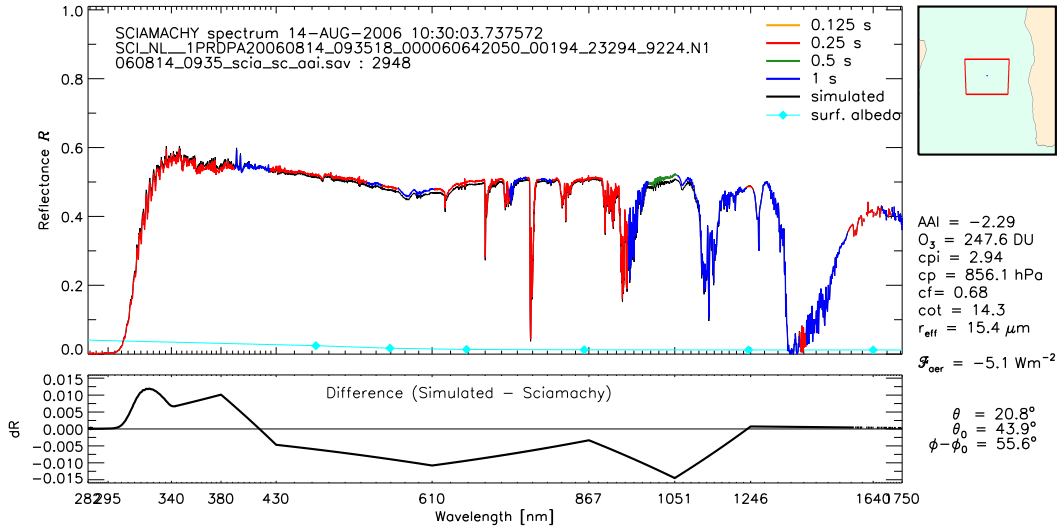

Figure 8: Simulated (black) and measured reflectance spectra of an aerosol-unpolluted water cloud scene on 14 August 2006 at 10:30:04 UTC at different ITs: 0.25 s (red), 0.5 s (green) and 1 s (blue). The absence of absorbing aerosols above the clouds was ensured by a negative value of the AAI of -0.8. This scene was characterised by a cloud phase index of 3, a cloud fraction of 0.7 and a cloud pressure of 856 hPa, indicating a low level marine cloud. The retrieved $\tau_{\rm cld}$ for this scene was 14.3, the $r_{\rm eff}$ was 15.4 μm. The simulated cloud spectrum for these cloud parameters, the scene geometry and a total ozone column of 248 DU, is shown in black. The modelled surface albedo is shown in cyan. The reflectance difference between the simulated and measured cloud scene is shown in the lower panel. The sampled scene is the blue spot in the middle of the red box over the South-Atlantic Ocean as shown in the inset.

that were sampled with an IT of 0.25 s, and co-added, are shown in red, parts that were sampled with an IT of 0.5 s, and co-added, are shown in green, and parts that were sampled with an IT of 1 s are shown in blue. The entire spectrum has an IT of 1 s. The absence of UV-absorbing aerosols was confirmed by a negative AAI value of -0.8. The FRESCO cloud fraction and cloud pressure were 0.7 and 856 hPa for this scene, respectively, indicating a marine low level cloud. The cloud optical thickness and droplet effective radius for this scene were 14.3 and 15.4 μm, respectively. The simulated unpolluted cloud reflectance spectrum using these parameters is shown in black. The difference between the simulated and measured reflectance spectra is plotted in the lower panel of Figure 8, and shows that the difference is in general very small (< 0.015) for this scene. The differences are well within the uncertainty of SCIAMACHY's reflectance measurements of about 3%. Apparently, an unpolluted cloud reflectance spectrum can be accurately extrapolated from the SWIR to the visible and the UV.

The differences between the modelled and measured spectra are caused by SCIAMACHY's measurement uncertainty and the errors in the retrieval of the cloud optical thickness and effective droplet size. Minor causes are interpolation errors in the LUT and possibly scattering by aerosols in the scene that cannot be distinguished from clouds. The latter errors are random, but SCIAMACHY measurement and $\tau_{\rm cld}$ and $r_{\rm eff}$ retrieval errors may be systematic. The presented case is typical for SCIAMACHY measurements of unpolluted water cloud spectra. A complete accuracy assessment and the consequences for the retrieval uncertainty are presented in *de Graaf et al.* [2012].

5.2. Polluted cloud spectra accuracy assessment

To fully understand the processes involved in the observed reflectances, model calculations were performed which simulate not only the unpolluted cloud scene, but also a polluted cloud scene. The cloud layer was simulated in a 1 km thick layer with variable optical thickness, simulated as before.

A Mie model for smoke was used with a refractive index at 550 nm of $1.54 - 0.018i$. This number was found for aged smoke during the SAFARI 2000 campaign [*Haywood et al.*, 2003] and was used for all wavelengths longer than 550 nm. However, for the UV spectral region the imaginary refractive

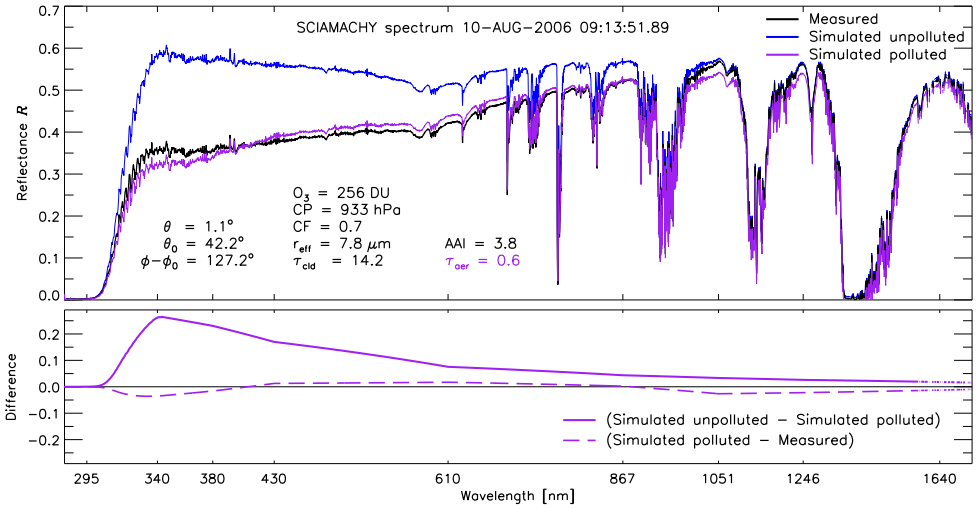

Figure 9: Top panel: modelled aerosol-polluted cloud reflectance spectrum (purple), together with the measured SCIAMACHY scene reflectance (black) and the modelled equivalent aerosol-unpolluted cloud reflectance spectrum (blue) on 10 August 2006 at 09:13:51.89 UTC. The optical thickness of the model aerosol layer $\tau_{\rm aer}$ was 0.6 at 550 nm. Bottom panel: Difference between the simulated and measured aerosol-polluted cloud reflectance spectra (dashed purple) and the difference between the simulated unpolluted and polluted cloud reflectance spectra (solid purple).

index was modified in line with recent studies that have indicated that biomass burning aerosols are characterised by a significant fraction of organic carbon (OC) [e.g. *Kirchstetter et al.*, 2004; *Bergstrom et al.*, 2007], which is produced mainly by incomplete combustion processes. The light absorbing efficiency of OC increases strongly with decreasing wavelength in the UV. In contrast, aerosols dominated by black carbon (BC) have wavelength independent refractive indices ('gray' aerosol). These aerosols are found more in industrial waste products, where combustion processes have been optimised. The wavelength dependence of the aerosol absorption is expressed by the absorption Ångström exponent, which is different for different types of aerosols. The absorption Ångström exponent for African biomass burning aerosols from SAFARI 2000 observations was found to be around 1.45 in the spectral region from 325 to 1000 nm [*Bergstrom et al.*, 2007; *Russell et al.*, 2010]. Satellite observations from OMI proved better fitted with aerosol models that had absorption Ångström exponents from 2.5 to 3 in the UV [*Jethva and Torres*, 2011]. The absorption Ångström exponent for the smoke model used here was 2.91 in the UV. This fitted the wavelength dependence of the reflectance spectrum well when applied in a model scene of smoke and clouds, see Figure 9. A bi-modal log-normal size distribution model was used, based on the 'very aged' (5 days) biomass plume found over Ascension Island during SAFARI 2000 [*Haywood et al.*, 2003]. The geometric radii for this haze plume used in the simulations here were $r_{\rm c} = 0.255$ μm and $r_{\rm f} = 0.117$ μm for the coarse and fine modes, with standard deviations $\sigma_{\rm c} = 1.4$ and $\sigma_{\rm f} = 1.25$, respectively. The fine mode number fraction was 0.9997.

The aerosol extinction optical thickness $\tau_{\rm aer}$ of the aerosol layer was fitted so that the total irradiance change of the modelled scene matched that of the measured scene. For a scene on 10 August 2006, at 09:13:52 UTC this yielded a $\tau_{\rm aer}$ of 0.6 at 550 nm, see Figure 9. The reflectance spectrum of this modelled scene is shown by the purple curve, while the measured reflectance spectrum is given in black and the modelled unpolluted cloud reflectance spectrum in blue. The differences between the modelled aerosol-polluted cloud scene and the measured and modelled unpolluted cloud scenes are given in the lower panel. The simulation follows the measurements closely over most of the spectral region, confirming the wavelength dependence of the smoke refractive index. Below about 400 nm the slope of the reflectance spectrum is slightly overestimated, so the absorption Ångström exponent should probably be smaller in this spectral region for this scene. The polluted cloud scene is analysed to assess the errors involved in adding aerosols to a cloud scene.

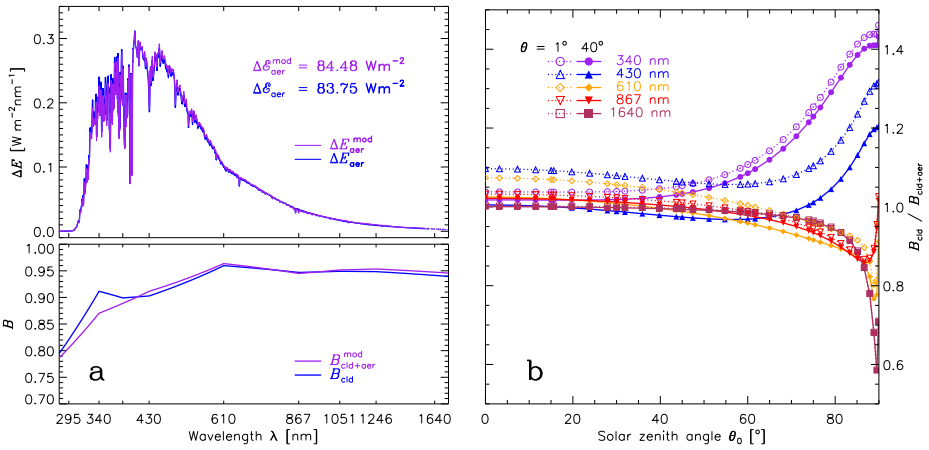

Figure 10: Changes in the anisotropy factor due to aerosols in the scene. a) Top panel: Net irradiance change (absorbed energy) as a function of wavelength for a scene on 10 August 2006 at 09:13:51.89 UTC. The blue curve shows the irradiance change using the anisotropy factor of the modelled aerosol-unpolluted cloud scene $B_{\rm cld}$ as in equation (10), while the purple curve shows the irradiance change with the actual (modelled) aerosol-polluted cloud scene anisotropy. Bottom panel: Anisotropy factor for the modelled unpolluted cloud scene $B_{\rm cld}$ (blue) and the modelled polluted cloud scene $B_{\rm cld+aer}$ (purple). b) Anisotropy change as a function of solar zenith angle for selected wavelengths due to the presence of the aerosols. The modelled scene was the same as in a). The dotted lines with open symbols show the anisotropy change for a viewing zenith angle of 1°. The solid line with filled symbols shows the anisotropy change for a viewing zenith angle of 40°.

5.3. Anisotropy factor

From the model results the anisotropy factor of the aerosol-polluted cloud scene $B_{\rm cld+aer}$ can now be determined for any geometry. For the scene shown in Figure 9 the anisotropy factor of the aerosol-polluted scene is slightly different from that of the aerosol-unpolluted cloud scene, see Figure 10a. As mentioned above, the optical thickness of the aerosol layer $\tau_{\rm aer}$ was fitted so that the aerosol DRE, using equation (10), was the same for the modelled aerosol-polluted cloud scene as for the measured scene (84 Wm^{-2}). When the actual anisotropy factor of the modelled aerosol-polluted cloud scene was used, as in equation (8), the aerosol absorption shifts slightly from the UV to more visible wavelengths (see top panel in Figure 10a). Since the peak of the solar irradiance is in the visible, the total aerosol DRE increased by 0.9% (from 83.75 to 84.48 Wm^{-2}).

A modelling study showed that the angular redistribution of scattered radiation by aerosols is dependent on $\tau_{\rm aer}$, wavelength and geometry. The dependence on $\tau_{\rm aer}$ is linear, with an increasing change for increasing $\tau_{\rm aer}$. The change in anisotropy as a function of solar zenith angle is given in Figure 10b for several wavelengths. It is relatively small at any wavelength and viewing zenith angle for solar zenith angles below 60°. For larger solar zenith angles the change can be larger.

5.4. Cloud optical thickness and droplet size retrieval

The cloud microphysical parameters cloud optical thickness $\tau_{\rm cld}$ and cloud droplet effective radius $r_{\rm eff}$ can be derived from the cloud scene reflectance in the visible and the SWIR. [*Nakajima and King*, 1990; *Platnick et al.*, 2003]. In Figure 11 the effect of absorbing aerosols on this retrieval of cloud microphysical parameters is shown, following *Haywood et al.* [2004]. The left panel shows the difference between the cloud microphysical retrievals for clean (black) and smoke polluted (white) clouds using the 867 nm and 1640 nm channels, which is the wavelength pair used for many instruments like Advanced Very High Resolution Radiometer (AVHRR) [*Kawamoto et al.*, 2001], Moderate Resolution Imaging Spectroradiometer (MODIS) [*Platnick et al.*, 2003], Spinning Enhanced Visible and Infrared Imager (SEVIRI) [*Roebeling et al.*, 2006] and SCIAMACHY by *Kokhanovsky et al.* [2005]. As was shown by *Haywood et al.* [2004], the TOA reflectance for a polluted cloud is lower than that for a clean cloud, due to the aerosol absorption. Therefore, without a correction for this effect, the retrieved cloud optical thickness and effective radius will be underestimated. The

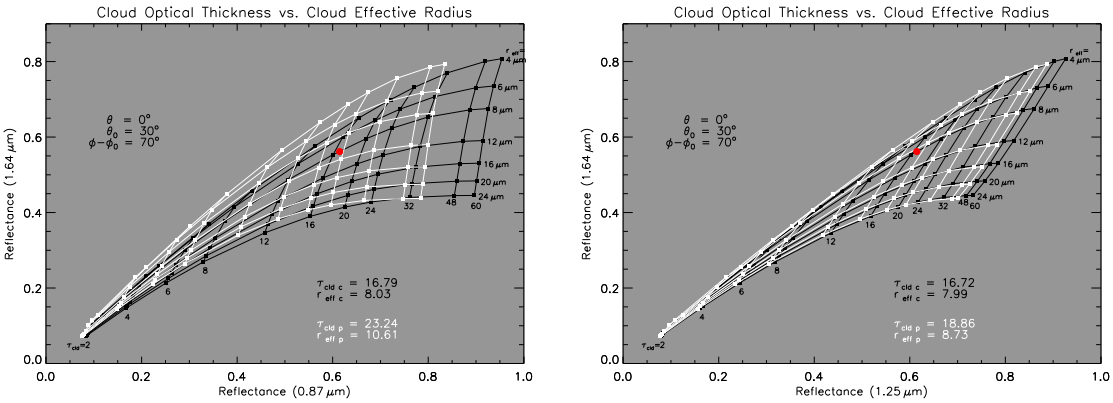

Figure 11: Clean cloud (black) and smoke polluted (white) TOA reflectances at one geometry (as given) using different channels: 867/1640 nm (left panel), and 1246/1640 nm (right panel).

right panel shows the effect of using the 1246/1640 nm wavelength pair instead of the 867/1640 nm wavelength pair. At 1246 nm the extinction coefficient is three times lower than at 867 nm and even only 11 % of that at 555 nm. Note that an aerosol optical thickness of 0.6 at 555 nm represents a dense smoke layer. Therefore, a retrieval algorithm was set up, to retrieve cloud parameters using SWIR wavelengths only, to minimise absorbing aerosol effects from smoke.

5.5. FRESCO retrievals

Using the modelled polluted cloud scene, the changes in FRESCO retrievals due to aerosol absorption were assessed. The change in FRESCO CP and FRESCO CF for increasing AOT is shown in Figure 12. FRESCO CF is increasingly affected by aerosol absorption, while FRESCO CP is affected only for AOT larger than about 1.5 at 550 nm. Since the maximum AOT for smoke over the South-Atlantic Ocean is about 1.5 at 532 nm [*Chand et al.*, 2009], the influence of aerosol absorption on the FRESCO CP retrieval is expected to be small. Furthermore, since cloud height has a small influence on the aerosol DRE, the error from FRESCO CP retrieval uncertainties can be neglected. The FRESCO CF is underestimated by about 0.2 for an AOT of 1.5 at 550 nm. Note that the AAI for an AOT of 1.5 at 550 nm is already as high as 9.

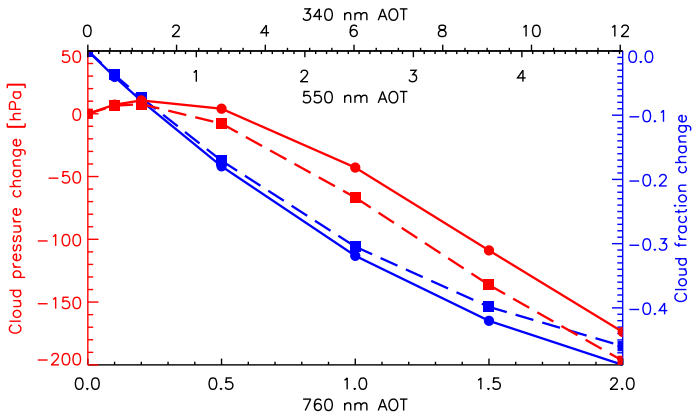

Figure 12: Change of FRESCO cloud pressure (red) and cloud fraction (blue) retrievals, for increasing aerosol load above a cloud at two solar zenith angles and nadir view. The x-axes show the AOT of the smoke layer at three different wavelengths. The water cloud, with a cloud optical thickness of 20, was placed between 1 and 2 km, while the absorbing smoke layer was placed between 4 and 5 km.

6. Conclusions

During project CLARIFI a completely new and innovative method was developed to retrieve the aerosol DRE over clouds using space-based spectrometer measurements and RTM results of cloud scene TOA reflectances. In order to avoid the difficulties in retrieving aerosol parameters from satellite instruments in general, and in cloudy scenes in particular, only cloud parameters are retrieved from the measurements, along with scene parameters that are needed to characterize the cloud reflectance spectrum. The latter include generally available parameters like scattering geometry, total ozone column and surface albedo. Cloud fraction and cloud height can be retrieved using the FRESCO algorithm, relatively unaffected by aerosol contamination. Cloud droplet effective radius $r_{\rm eff}$ and cloud optical thickness $\tau_{\rm cld}$ can be retrieved in the SWIR with also well-established algorithms used for MODIS and SEVIRI, among others. However, special care must be taken when retrieving these parameters in aerosol contaminated cloud scenes. Absorption by aerosols in the cloud retrieval bands can bias the retrieved cloud parameters, which is relevant in the current context. Therefore, the cloud parameters are retrieved as far in the SWIR as possible, where the aerosol extinction optical thickness $\tau_{\rm aer}$ becomes negligible. Aerosols attenuate the radiation most efficiently at wavelengths comparable to their own sizes. This means that a retrieval of $r_{\rm eff}$ and $\tau_{\rm cld}$ at wavelengths away from the optically active range of the aerosols will be optimal.

With the retrieved cloud and scene parameters a reflectance spectrum can be simulated for an aerosol-unpolluted cloud scene. This reflectance spectrum can be compared with the measured reflectance and the aerosol DRE can be determined for any water cloud scene for which the reflectance spectrum is measured in the solar spectral range, while aerosol microphysical property assumptions and retrievals are avoided. The differences between the spectra can be attributed directly to aerosol absorption, although scattering effects may also remove or add radiation in the viewing direction. The latter effect is indicated by a change in anisotropy factor, which was shown to be small compared to the reduction in the reflectance due to absorption, for smoke.

The aerosol DRE over clouds from SCIAMACHY was averaged for all cloudy scenes in a box over the South-Atlantic Ocean in August 2006. During this period an extensive biomass burning aerosol plume was advected from the African mainland over a permanent marine boundary layer cloud deck. The maximum aerosol DRE found during this period in a single pixel was $132 \pm 8\,\mathrm{Wm}^{-2}$. Such high values were also found in the reduction of shortwave flux from CERES in areas with high TOMS AI near China [*Hsu et al.*, 2003]. The regionally and monthly averaged aerosol DRE over clouds in August 2006 was 23 ± 8 Wm^{-2} with a variation over the region in this month of 22 Wm^{-2}.

SCIAMACHY's 0.25 s pixels have a spatial resolution of approximately $60 \times 30\,\mathrm{km}^2$, and global coverage is reached once every six days. Although with this design SCIAMACHY does not have an optimal spatial resolution, the averaged retrieved aerosol DRE over clouds shows unprecedented details. The aerosol DRE over clouds is dependent on cloud cover and aerosol presence, which are both highly variable. SCIAMACHY has been measuring successfully since mid-2002, which can be used to retrieve time series of the aerosol DRE over clouds and relate this to changes in cloud cover and aerosol presence.

To retrieve the aerosol DRE at an even higher spatial resolution, the method presented here for SCIAMACHY may be used for other instruments as well. For example, MODIS and OMI, flying in the A-Train constellation, may be used to retrieve cloud parameters in the SWIR (from MODIS), while spectral UV reflectance measurements from OMI can be used to determine the aerosol absorption. The spectral range of OMI covers only the wavelength region up to 500 nm, but the current study shows that this will suffice to capture the bulk of the absorbed energy in the solar spectrum. The reflectance spectrum in the visible and SWIR may be estimated using the few reflectance measurements from MODIS at longer wavelengths. With a precomputed cloud reflectance LUT at OMI/MODIS wavelengths the aerosol DRE in cloud scenes may then be estimated at a superior spatial resolution.

The use of retrieved cloud optical thickness and cloud droplet effective radius to construct a (water cloud) reflectance spectrum implies an implicit separation of the aerosol DRE in cloudy scene from that in clear skies. This is one of the areas where observations of aerosol DRE are currently lacking [*Yu et al.*, 2006; *Forster et al.*, 2007]. Consequently, the method presented here can complement studies that retrieve aerosol parameters in clear-sky only. The latter may be used to derive the aerosol DRE in clear-skies.

Acknowledgements

CLARIFI was funded by the European Space Agency (ESA) within the Support to Science Element, project number 22403. Personal note: MdG wishes to thank D. Fernández Prieto, S. Dransfeld, B. Bojkov and R. Sabia at ESA Esrin for their personal help and support during the project.

References

Abel, S. J., H. J. Highwood, J. M. Haywood, and M. A. Stringer, The direct radiative effect of biomass burning aerosols over southern Africa, *Atmos. Chem. Phys.*, *5*, 2005.

Anderson, G. P., S. A. Clough, F. X. Kneizys, J. H. Chetwynd, and E. P. Shettle, AFGL atmospheric constituent profiles, *Tech. Rep. AFGL-TR-86-0110*, Air Force Geophysics Laboratory, 1986.

Bergstrom, R. W., P. Pilewskie, P. B. Russell, J. Redemann, T. C. Bond, P. K. Quinn, and B. Sierau, Spectral absorption properties of atmospheric aerosols, *Atmos. Chem. Phys.*, *7*(23), 5937–5943, doi:10.5194/acp-7-5937-2007, 2007.

Chand, D., T. L. Anderson, R. Wood, R. J. Charlson, Y. Hu, Z. Liu, and M. Vaughan, Quantifying above-cloud aerosol using spaceborne lidar for improved understanding of cloud-sky direct climate forcing, *J. Geophys. Res.*, *113*, D13206, doi:10.1029/2007JD009433, 2008.

Chand, D., R. Wood, T. L. Anderson, S. K. Satheesh, and R. J. Charlson, Satellite-derived direct radiative effect of aerosols dependent on cloud cover, *Nat. Geosci.*, *2*, doi:10.1038/NGEO437, 2009.

Chandrasekhar, S., *Radiative Transfer*, 393 pp., Dover, Mineola, N.Y., 1960.

Costantino, L., and F. -M. Bréon, Analysis of aerosol-cloud interaction from multi-sensor satellite observations, *Geophys. Res. Lett.*, *37*, L11801, doi:10.1029/2009GL041828, 2010.

de Graaf, M., P. Stammes, O. Torres, and R. B. A. Koelemeijer, Absorbing Aerosol Index: Sensitivity Analysis, application to GOME and comparison with TOMS, *J. Geophys. Res.*, *110*, D01201, doi:10.1029/2004JD005178, 2005.

de Graaf, M., P. Stammes, and E. A. A. Aben, Analysis of reflectance spectra of UV-absorbing aerosol scenes measured by SCIAMACHY, *J. Geophys. Res.*, *112*, D02206, doi: 10.1029/2006JD007249, 2007.

de Graaf, M., L. G. Tilstra, P. Wang, and P. Stammes, Retrieval of the aerosol direct radiative effect over clouds from space–borne spectrometry, *J. Geophys. Res.*, *117*, in press, doi: 10.1029/1029/2004JD005178, 2012.

De Haan, J. F., P. B. Bosma, and J. W. Hovenier, The adding method for multiple scattering calculations of polarized light, *Astron. Astrophys.*, *183*, 371–391, 1987.

Diner, D. J., et al., MISR aerosol optical depth retrievals over Southern Africa during the SAFARI-2000 dry season campaign, *Geophys. Res. Lett.*, *28*(6), 3127–3130, doi:10.1029/2001GL013188, 2001.

Forster, P., et al., Contribution of working group I to the fourth assessment report of the intergovernmental panel on climate change, in *Climate Change 2007: The Physical Science Basis.*, edited by S. Solomon, D. Qin, M. Manning, Z. Chen, M. Marquis, K. Averyt, M. Tignor, and H. Miller, p. 996, Cambridge Univ. Press, Cambridge, UK and New York, NY, USA, 2007.

Hansen, J. E., Multiple Scattering of Polarized Light in Planetary Atmospheres. Part II. Sunlight Reflected by Terrestrial Water Clouds, *J. Atmos. Sci.*, *28*, 1400 – 1426, 1971.

Hauser, A., D. Oesch, N. Foppa, and S. Wunderle, NOAA AVHRR derived aerosol optical depth over land, *J. Geophys. Res.*, *110*, D08204, doi:10.1029/2004JD005439, 2005.

Haywood, J., and O. Boucher, Estimates of the direct and indirect radiative forcing due to tropospheric aerosols: A review, *Rev. Geophys.*, *38*(4), 513–543, 1999RG000078, 2000.

Haywood, J. M., S. R. Osborne, P. N. Francis, A. Neil, P. Formenti, M. O. Andreae, and P. H. Kaye, The mean physical and optical properties of regional haze dominated by biomass burning aerosol measured from the C–130 aircraft during SAFARI 2000, *J. Geophys. Res.*, *108*, D13, doi: 10.1029/2002JD002226, 2003.

Haywood, J. M., S. R. Osborne, and S. J. Abel, The effect of overlying absorbing aerosol layers on remote sensing retrievals of cloud effective radius and cloud optical depth, *Q. J. R. Meteorol. Soc.*, *130*, 779–800, doi:10.1256/qj.03.100, 2004.

Herman, J. R., P. K. Bhartia, O. Torres, C. Hsu, C. Seftor, and E. A. Celarier, Global distributions of UV-absorbing aerosols from NIMBUS 7/TOMS data, *J. Geophys. Res.*, *102*, D14, doi: 10.1029/96JD03680, 1997.

Hsu, N. C., J. R. Herman, and S. Tsay, Radiative impacts from biomass burning in the presence of clouds during boreal spring in southeast Asia, *Geophys. Res. Lett.*, *30*(5), 1224, doi: 10.1029/2002GL016485, 2003.

Jethva, H., and O. Torres, Satellite-based evidence of wavelength-dependent aerosol absorption in biomass burning smoke inferred from Ozone Monitoring Instrument, *Atmos. Chem. Phys.*, *11*, 10,541–10,551, doi:10.5194/acp-11-10541-2011, 2011.

Johnson, B. T., K. P. Shine, and P. M. Forster, The semi–direct aerosol effect: Impact of absorbing aerosols on marine stratocumulus, *Q. J. R. Meteorol. Soc.*, *130*, 1407–1422, doi:10.1256/qj.03.61, 2004.

Kawamoto, K., T. Nakajima, and T. Y. Nakajima, A global determination of cloud microphysics with AVHRR remote sensing, *J. Climate*, *14*(9), 2054–2068, doi:10.1175/1520-0442, 2001.

Keil, A., and J. M. Haywood, Solar radiative forcing by biomass burning aerosol particles during SAFARI 2000: A case study based on measured aerosol and cloud properties, *J. Geophys. Res.*, *108*, D13, doi:10.1029/2002JD002315, 2003.

King, M. D., Cloud and Aerosol Properties, Precipitable Water, and Profiles of Temperature and Water Vapor from MODIS, *IEEE Trans. Geosci. Remote Sens.*, *41*(2), 442–458, 2003.

Kirchstetter, T. W., T. Novakov, and P. V. Hobbs, Evidence that the spectral dependence of light absorption by aerosols is affected by organic carbon, *J. Geophys. Res.*, *109*, D21208, doi: 10.1029/2004JD004999, 2004.

Knobelspiesse, K., B. Cairns, J. Redemann, R. W. Bergstrom, and A. Stohl, Simultaneous retrieval of aerosol and cloud properties during the MILAGRO field campaign, *Atmos. Chem. Phys.*, *11*(13), 6245–6263, 2011.

Kokhanovsky, A. A., V. V. Rozanov, J. P. Burrows, K.-U. Eichmann, W. Lotz, and M. Vountas, The SCIAMACHY cloud products: Algorithms and examples from ENVISAT, *Adv. Space Res.*, *36*, 789–799, doi:10.1016/j.asr.2005.03.026, 2005.

Liou, K. N., *An Introduction to Atmospheric Radiation*, 583 pp., Academic Press, 2002.

Lohmann, U., and J. Feichter, Global indirect aerosol effects: a review, *Atmos. Chem. Phys.*, *5*, 2005.

Myhre, G., T. K. Berntsen, J. M. Haywood, J. K. Sundet, B. N. Holben, M. Johnsrud, and F. Stordal, Modeling the solar radiative impact of aerosols from biomass burning during the southern african regional science initiative (SAFARI-2000) experiment, *J. Geophys. Res.*, *108*, D13, doi:10.1029/2002JD002313, 2003.

Nakajima, T., and M. D. King, Determination of the Optical Thickness and Effective Particle Radius of Clouds from Reflected Solar Radiation Measurements: Part I: Theory, *J. Atmos. Sci.*, *47*(15), 1990.

Peters, K., J. Quaas, and N. Bellouin, Effects of absorbing aerosols in cloudy skies: a satellite study over the atlantic ocean, *Atmos. Chem. Phys.*, *11*, 1393–1404, doi:10.5194/acp-11-1393-2011, 2011.

Platnick, S., M. D. King, S. A. Ackerman, W. P. Menzel, B. A. Baum, J. C. Riédi, and R. A. Frey, The MODIS Cloud Products: Algorithms and Examples From Terra, *IEEE Trans. Geosci. Remote Sens.*, *41*(2), 459–473, 2003.

Redemann, J., Q. Zhang, P. B. Russel, J. M. Livingston, and L. A. Remer, Case studies of aerosol remote sensing in the vicinity of clouds, *J. Geophys. Res.*, *114*, doi:10.1029/2008JD010774, 2009.

Roebeling, R. A., A. J. Feijt, and P. Stammes, Cloud property retrievals for climate monitoring: Implications of differences between Spinning Enhanced Visible and Infrared Imager (SEVIRI) on METEOSAT-8 and Advanced Very High Resolution Radiometer (AVHRR) on NOAA-17, *J. Geophys. Res.*, *111*, D20210, doi:10.1029/2005JD006990, 2006.

Russell, P. B., et al., Absorption Angstrom Exponent in AERONET and related data as an indicator of aerosol composition, *Atmos. Chem. Phys.*, *10*(3), 1155–1169, doi:10.5194/acp-10-1155-2010, 2010.

Sakaeda, N., R. Wood, and P. J. Rasch, Direct and semidirect aerosol effects of southern african biomass aerosol, *J. Geophys. Res.*, *116*, doi:10.1029/2010JD015540, 2011.

Stammes, P., Spectral radiance modelling in the UV-visible range, in *IRS 2000: Current problems in atmospheric radiation*, edited by W. Smith and Y. Timofeyev, pp. 385–388, A. Deepak Publishing, Hampton (VA), 2001.

Swap, R. J., M. Garstang, S. A. Macko, P. D. Tyson, W. Maenhaut, P. Artaxo, P. Kållberg, and R. Talbot, The long-range transport of southern African aerosols to the tropical South Atlantic, *J. Geophys. Res.*, *101*, D19, doi:10.1029/95JD01049, 1996.

Tanré, D., M. Herman, and Y. J. Kaufman, Information on aerosol size distribution contained in solar reflected spectral radiances, *J. Geophys. Res.*, *101*, D14, doi:10.1029/96JD00333, 1996.

Tilstra, L. G., M. de Graaf, I. Aben, and P. Stammes, In-flight degradation correction of SCIAMACHY UV reflectances and Absorbing Aerosol Index, *J. Geophys. Res.*, *117, in press*, doi: 10.1029/2011JD016957, 2011.

Torres, O., P. K. Bhartia, J. R. Herman, Z. Ahmad, and J. Gleason, Derivation of aerosol properties from satellite measurements of backscattered ultraviolet radiation: Theoretical basis, *J. Geophys. Res.*, *103*, D14, doi:10.1029/98JD00900, 1998.

Torres, O., P. K. Bhartia, J. R. Herman, A. Sinyuk, P. Ginoux, and B. Holben, A long-term record of aerosol optical depth from TOMS observations and comparison to AERONET measurements, *J. Atmos. Sci.*, *59*(3), 398–413, doi:10.1175/1520-0469, 2002.

Torres, O., A. Tanskanen, B. Veihelmann, C. Ahn, R. Braak, P. K. Bhartia, P. Veefkind, and P. Levelt, Aerosols and surface UV products from Ozone Monitoring Instrument observations: An overview, *J. Geophys. Res.*, *112*, D24S47, doi:10.1029/2007JD008809, 2007.

Tummon, F., F. Solmon, C. Liousse, and M. Tadross, Simulation of the direct and semidirect aerosol effects on the southern Africa regional climate during the biomass burning season, *J. Geophys. Res.*, *115*, D19206, doi:10.1029/2009JD013738, 2010.

Veefkind, J. P., G. de Leeuw, P. Stammes, and R. B. A. Koelemeijer, Regional Distribution of Aerosol over Land, Derived from ATSR-2 and GOME, *Remote Sens. Environ.*, *74*, 377–386, 2000.

Waquet, F., J. Riedi, L. C. Labonnote, P. Goloub, B. Cairns, J. -L. Deuzé, and D. Tanré, Aerosol Remote Sensing over Clouds Using A-Train Observations, *J. Atmos. Sci.*, *66*, doi: 10.1175/2009JAS3026.1, 2009.

Wilcox, E. M., Stratocumulus cloud thickening beneath layers of absorbing smoke aerosol, *Atmos. Chem. Phys.*, *10*(23), 11,769–11,777, 2010.

Wilcox, E. M., Direct and semi-direct radiative forcing of smoke aerosols over clouds, *Atmos. Chem. Phys. Disc.*, *11*, 20,947–20,972, 2011.

Yu, H., et al., A review of measurement-based assessments of the aerosol direct radiative effect and forcing, *Atmos. Chem. Phys.*, *6*(3), 613–666, doi:10.5194/acp-6-613-2006, 2006.

A complete list of all KNMI-publications (1854 – present) can be found on our website

www.knmi.nl/knmi-library/knmipub_en.html

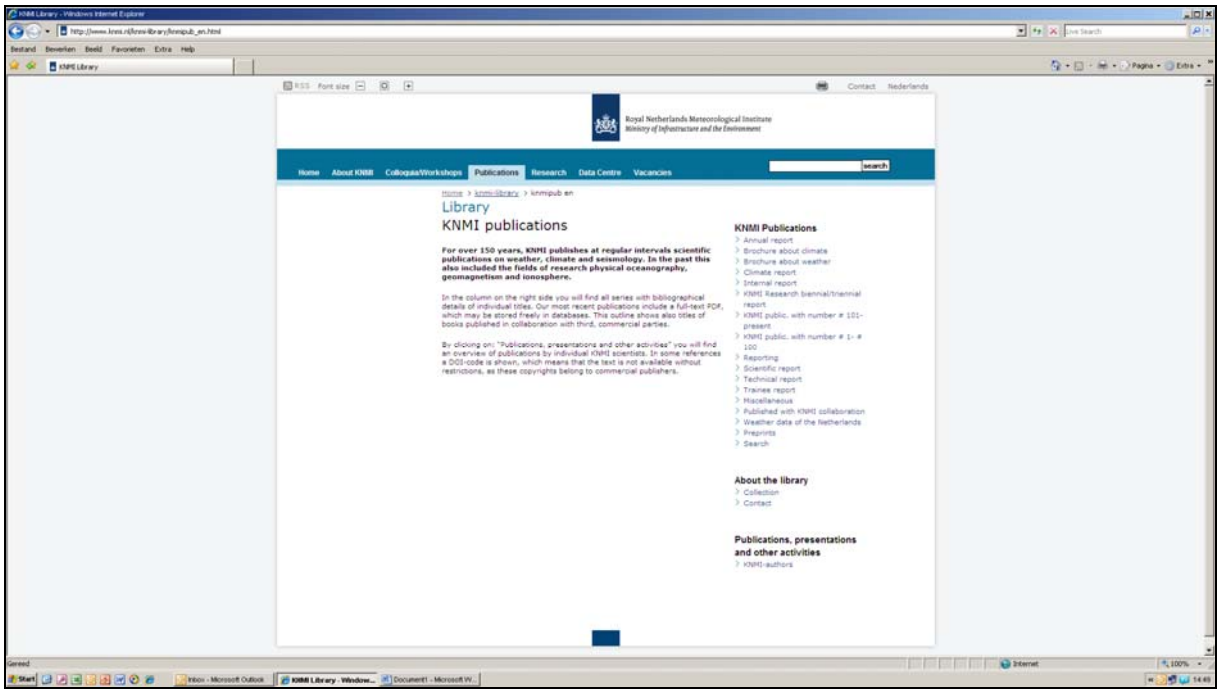

The most recent reports are available as a PDF on this site.